

PR-MIM: Delving Deeper into Partial Reconstruction in Masked Image Modeling

Zhong-Yu Li¹ Yunheng Li¹ Deng-Ping Fan¹ Ming-Ming Cheng¹

¹VCIP, School of Computer Science, Nankai University

Abstract

Masked image modeling has achieved great success in learning representations but is limited by the huge computational costs. One cost-saving strategy makes the decoder reconstruct only a subset of masked tokens and throw the others, and we refer to this method as partial reconstruction. However, it also degrades the representation quality. Previous methods mitigate this issue by throwing tokens with minimal information using temporal redundancy inaccessible for static images or attention maps that incur extra costs and complexity. To address these limitations, we propose a progressive reconstruction strategy and a furthest sampling strategy to reconstruct those thrown tokens in an extremely lightweight way instead of completely abandoning them. This approach involves all masked tokens in supervision to ensure adequate pre-training, while maintaining the cost-reduction benefits of partial reconstruction. We validate the effectiveness of the proposed method across various existing frameworks. For example, when throwing 50% patches, we can achieve lossless performance of the ViT-B/16 while saving 28% FLOPs and 36% memory usage compared to standard MAE. Our source code will be made publicly available.

1. Introduction

Masked image modeling (MIM), which optimizes representations by masking a part of tokens and predicting them, has significantly promoted representation learning. However, it usually demands substantial computational resources, e.g., a long pre-training schedule of 1600 epochs [24]. Recently, partial reconstruction [38, 39, 53] has been proposed to reduce the costs by throwing a subset of masked tokens, where these thrown tokens are not reconstructed and involved in the loss calculation, thereby reducing computational overhead. However, this approach also degrades the quality of learned representations, as shown in Fig. 1, especially for large models, as shown in our experiments.

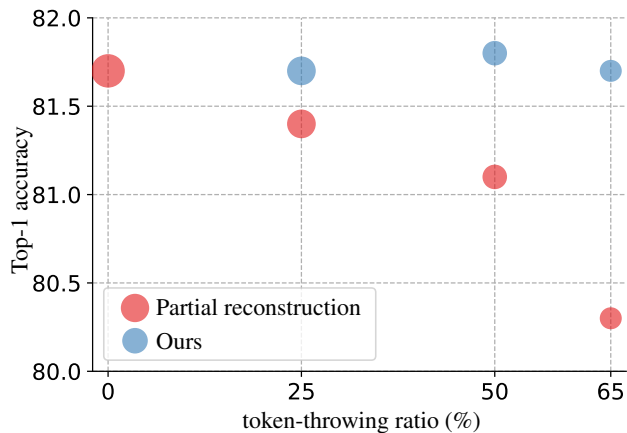


Figure 1. Performance on ImageNet-1K. The bubble area is proportional to the training FLOPs. A higher throwing ratio indicates more tokens are thrown with lower training costs but leads to greater degradation in plain partial reconstruction.

Some strategies have been proposed to address the above issue but are insufficient for MIM. For instance, in masked video modeling (MVM), VideoMAE V2 [53] leverages temporal redundancy to throw tokens that are repeated across adjacent frames, effectively mitigating the adverse effects of partial reconstruction in MVM. However, the temporal redundancy is inaccessible for static images. In MIM, [38, 39] utilize attention maps to throw the tokens with low attention scores. However, it requires running a pre-trained transformer on the complete token sequence and consumes storage space, which contradicts the goal of partial reconstruction to reduce costs. Moreover, these methods cannot eliminate the degradation when applying partial reconstruction to some MIM frameworks like SimMIM [62]. Instead, we aim to bridge the performance gap while preserving the training efficiency of partial reconstruction and apply our method to various MIM frameworks.

Partial reconstruction throws a part of tokens that can contribute to effective supervision, thus reducing the effective epochs and the accuracy of gradients estimated in stochastic gradient descent. Thus, we propose a progressive

reconstruction scheme to reconstruct the tokens thrown by partial reconstruction, allowing them to contribute to model supervision. After the decoder first reconstructs the tokens retained by partial reconstruction, we use an extremely lightweight spatial aggregation module to reconstruct the thrown tokens based on those retained tokens. This spatial aggregation requires negligible $7.3 \cdot 10^{-3}$ G floating-point operations per second (FLOPS) and increases almost no costs. Experiments show that this approach mitigates the performance degradation caused by partial reconstruction and yields reasonable reconstruction results. Furthermore, we observe an unfavorable situation, *i.e.*, there may be too few retained tokens surrounding a thrown token. This phenomenon is not conducive to effectively reconstructing this thrown token. Thus, we propose a furthest sampling strategy, which maximizes the spatial dispersion of the tokens retained by partial reconstruction, to reduce the occurrence of this situation. Moreover, this operation can be integrated into the multi-threaded data augmentation process, thus not impeding training speed.

In this work, we integrate the proposed method with different frameworks, including MAE [24], SimMIM [62], TEC [18], GreenMIM [29], LocalMIM [52], and MFF [36]. Through experiments with different model sizes, training schedules, and token-throwing ratios, we demonstrate that the proposed method can mitigate the performance degradation caused by partial reconstruction, as shown in Fig. 1. For example, compared to MAE, when training the ViT-B/16 for 800 epochs and throwing 50% tokens, we achieve consistent performance on various downstream tasks with only 72% GFLOPs, 75% pre-training time, and 64% memory usage. Further reduction can be achieved by throwing more tokens without sacrificing the performance.

In summary, our main contributions include: 1) We design the progressive reconstruction and the furthest sampling strategy to mitigate the performance degradation caused by partial reconstruction while keeping its ability to save costs, 2) The proposed method can significantly reduce the costs without sacrificing performance, facilitating the development of efficient representation learning framework, and 3) Our method is orthogonal to various methods, and we validate its effectiveness on various downstream tasks.

2. Related works

Self-supervised learning. Self-supervised learning (SSL) learns rich representations without relying on human annotations. Early works try different pretext tasks, *e.g.*, coloration [32, 66], jigsaw puzzles [40], rotation [19], autoencoder [12], inpainting [42], and counting [41], but these methods only achieve unsatisfactory performance. The recent success is partly due to the rapid development of instance discrimination. Assuming that representations should be invariant to image transforming, these

methods [16, 31, 43, 59, 67, 70] pull representations extracted from different views of an image closer. In this framework, different classical methods propose different strategies to avoid model collapse and guarantee the quality of learned representations, *e.g.*, contrastive learning with negative samples [7, 23, 25, 55], asymmetric architecture [8, 21, 47, 61], feature decoupling [17, 63, 65], and uniform distribution over channels [4, 5]. Some works also try different forms of representations in SSL, including self-relation [35] and category assignment [1, 4, 5]. Due to the increasingly powerful computing devices, these methods achieve excellent results on various vision tasks but require significant costs.

Masked image modeling. Inspired by masked language modeling [11], masked image modeling (MIM) [3, 24, 33, 46, 58] has successfully developed to learn image representations. MIM demonstrates superior performance by masking a subset of tokens and then reconstructing them based on the representations encoded from the unmasked tokens. The development of MIM is accompanied by the continuous optimization of reconstruction targets, which influences the properties of the learned representations. For example, many works [24, 36, 48, 51, 62] use pixel values as the target. The hand-designed HOG feature [10, 56] and frequency feature [60] have proven to be more effective targets than pixels. Many methods further attempt to extract representations from pre-trained models as the reconstruction target, including the pre-trained tokenizer in [3, 14, 54], pre-trained representation encoder in [18, 57], and siamese network in [2, 9, 13, 30, 45]. Some works [45, 64, 69] also take contrastive representations as the target to integrate the advantage of instance discrimination into MIM. Unlike instance discrimination, which requires multiple views of an image, MIM operates on a single view, allowing for larger batch size and faster training. However, the costs are still huge. In this work, we focus on leveraging partial reconstruction to save costs while avoiding the issue that partial reconstruction degrades the quality of representations.

3. Method

3.1. Preliminary

Masked image modeling. Masked image modeling (MIM) learns representations by masking a subset of tokens and then reconstructing the masked tokens based on the unmasked tokens. MIM has various implementations and we take the asymmetric encoder-decoder design in MAE [24] as an example to illustrate our method. Specifically, following ViT [15], an image is first divided into a sequence of regular non-overlapping tokens $x \in \mathbb{R}^{N \times C}$, where N is the number of patches and C is the number of dimensions. Then, a masking operation randomly masks $N \cdot \rho_e$ tokens and feeds the remaining $x_u \in \mathbb{R}^{N \cdot (1-\rho_e) \times C}$ into an

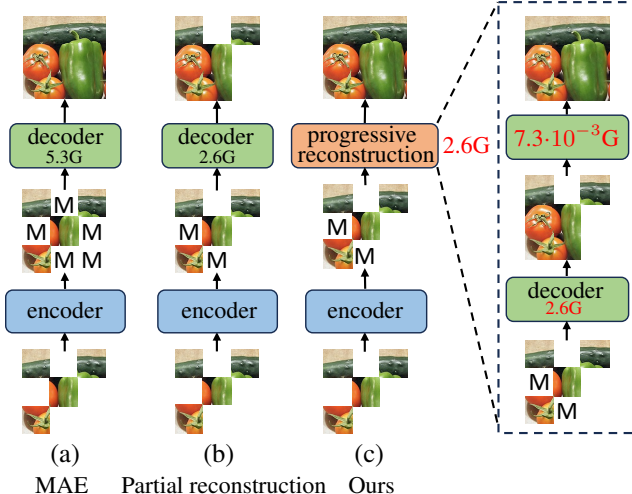


Figure 2. Different strategies for masked image modeling and the corresponding FLOPs of the decoder. Partial reconstruction throws a part of masked tokens x_t and retains the others x_d (marked by M), while our progressive reconstruction scheme proposed in Sec. 3.2 reconstructs the thrown tokens with minimal computational costs to ensure adequate training.

encoder to extract representations, where ρ_e is the masking ratio and typically set to 75% [24]. As shown in Fig. 2 (a), the decoder takes representations encoded in x_u and a trainable [MASK] token as input, where the [MASK] token is copied $N \cdot \rho_e$ times and then placed in the positions of masked tokens. In the decoder, the masked tokens are reconstructed by aggregating representations of unmasked tokens x_u , prompting the encoder to extract rich context information. In inference and fine-tuning, the encoder is used, and the decoder is removed.

Partial reconstruction. Partial reconstruction [38, 39, 53] has recently been utilized to reduce the computational costs of MIM by throwing a subset of masked tokens and only reconstructing the remaining ones, as shown in Fig. 2 (b). For simplicity, we define ρ_d as the token-throwing ratio, meaning a subset of masked tokens $x_t \in \mathbb{R}^{N \cdot \rho_d \times C}$ are thrown. This operation allows the decoder to operate on 1) unmasked tokens $x_u \in \mathbb{R}^{N \cdot (1 - \rho_e) \times C}$ and 2) masked but unthrown tokens $x_d \in \mathbb{R}^{N \cdot (\rho_e - \rho_d) \times C}$, with $N \cdot (1 - \rho_d)$ tokens. Thus, it accelerates pre-training, especially for transformer-based architectures where the attention mechanism exhibits quadratic complexity to the sequence length.

3.2. Progressive reconstruction scheme

While reducing costs, partial reconstruction only leverages a subset of tokens to supervise models in each training iteration, reducing the number of effective epochs and making the mini-batch-level stochastic gradient estimation less accurate. In this work, we propose a progressive reconstruction scheme that consists of a common decoder described

Sym.	Dim.	Meaning
N	scalar	number of tokens
ρ_e	scalar	masking ratio
ρ_d	scalar	throwing ratio
x	$N \times C$	patch tokens, $x = x_u \cup x_d \cup x_t$
x_u	$N \cdot (1 - \rho_e) \times C$	unmasked tokens
x_d	$N \cdot (\rho_e - \rho_d) \times C$	masked and unthrown tokens
x_t	$N \cdot \rho_d \times C$	masked and thrown tokens

Table 1. Table of symbols, their dimensions, and meaning.

in [24] and an extremely lightweight spatial aggregation module, where the former throws a subset of masked tokens and the latter reconstructs the thrown tokens in a simple yet effective manner, as shown in Fig. 2 (c). The framework of our method is demonstrated in Fig. 3.

Spatial aggregation. In the decoder, the unthrown masked tokens x_d are reconstructed by acquiring context information from the unmasked tokens x_u . We also reconstruct the thrown masked tokens x_t by aggregating the information from x_u and x_d . Differently, channel-level modeling, *e.g.*, FFN, is not required because the decoder has mapped the x_u and x_t to the space of reconstruction targets. Moreover, we aim to design a spatial aggregation module as simple and efficient as possible to save computational costs. In experiments, we show that a simple depth-wise convolution is enough to reconstruct x_t .

Specifically, given x_u and x_d from the decoder output, we first fill the thrown tokens x_t with zero values and rearrange all tokens from sequence to spatial format. Then, we apply a 7×7 depth-wise convolution to reconstruct the thrown tokens by aggregating information from x_u and x_d output by the decoder, with negligible $7.3 \cdot 10^{-3}$ GFLOPs. Then, we predict the pixel values of each masked token using a normalization layer and a linear layer, as described in [24]. In this way, involving each masked token in supervision can ensure adequate training and estimate gradients more accurately. As shown in Fig. 4, there is a large deviation between the gradient estimated by partial reconstruction and standard MAE, especially when using a large throwing ratio. In contrast, our PR-MIM can significantly alleviate this problem.

3.3. Furthest sampling

To reconstruct each thrown masked token in x_t , it is essential to ensure that there are enough tokens from x_u and x_d within a 7×7 region around each token in x_t , enabling each token in x_t to aggregate sufficient context information. However, this requirement is not ensured when randomly throwing tokens. Especially when there is no token of x_u and x_d around a token in x_t , as shown in Fig. 5 (left),

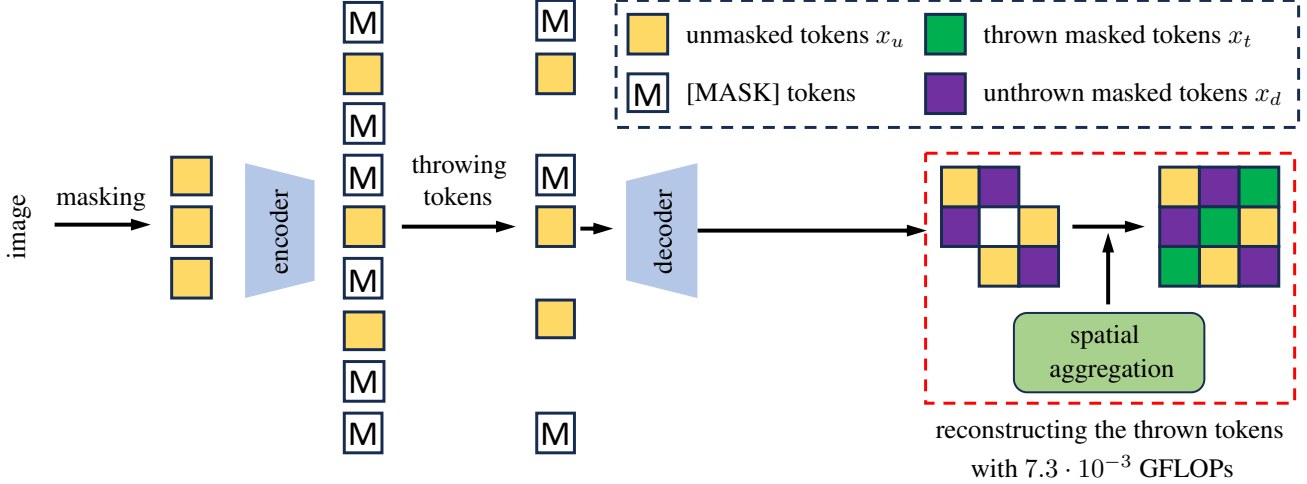


Figure 3. When partial reconstruction throws a subset of masked tokens, the proposed progressive reconstruction scheme reconstructs each masked token with minimal additional costs.

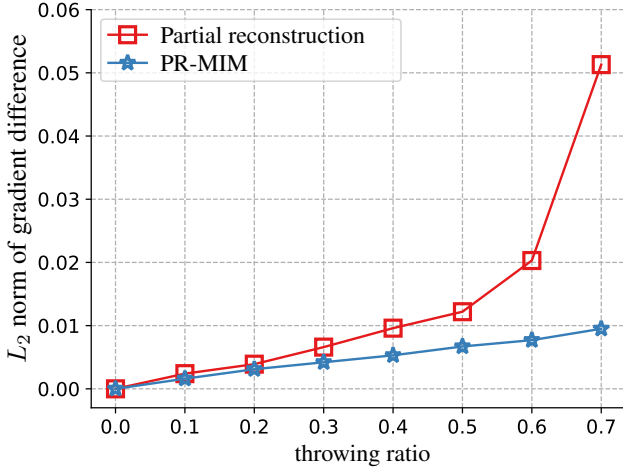


Figure 4. The L_2 norm of gradient difference between different methods and standard MAE.

we cannot calculate the meaningful loss on this token. A straightforward manner to overcome this issue is to enlarge the receptive field of the spatial aggregation module. However, experiments in Tab. 11 show that an excessive receptive field is sub-optimal, and previous works [6] have shown that a token is reconstructed by aggregating local information. To address this issue, we adopt a furthest sampling strategy, which selects the unthrown tokens x_d as dispersedly distributed as possible, as shown in Fig. 5 (right).

Suppose there are $N_m = N \cdot \rho_e$ masked tokens, and we throw $N_t = N \cdot \rho_d$ tokens among them. For illustration, we define $\mathbf{D} \in \mathbb{R}^{N_m \times N_m}$ as the distance matrix, where \mathbf{D}_{ij} is the distance between the i -th and j -th masked tokens. In this work, we use the Euclidean metric to measure distances because it requires minimal computational costs. The result

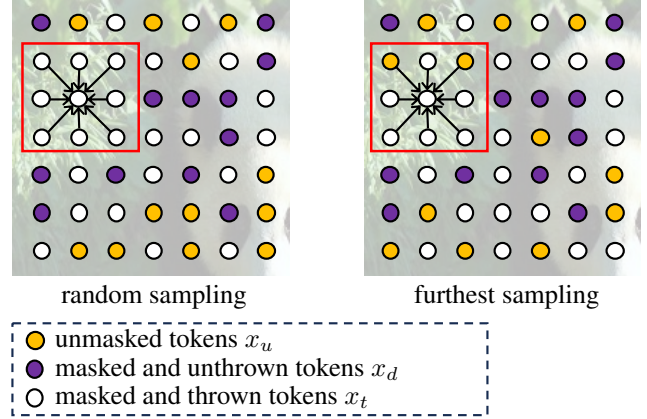


Figure 5. The furthest sampling strategy. The red box and arrows mean that the thrown token at the center is reconstructed by aggregating information from the other tokens within the box.

of token-throwing is denoted as $\mathbf{s} \in \mathbb{R}^{N_m}$. $\mathbf{s}_i = 1$ means the i -th masked token is retained, and $\mathbf{s}_i = 0$ means it is thrown. The furthest sampling finds the solution as follows:

$$\max_{\mathbf{s}} \sum_{i=0}^{N_m-1} \sum_{j=0}^{N_m-1} \mathbb{1}(s_i = 1 \wedge s_j = 1) \cdot \mathbf{D}_{ij}, \quad (1)$$

$$\text{s.t.} \quad \sum_{i=0}^{N_m} s_i = N_m - N_t, \quad (2)$$

$$s_i \in \{0, 1\} \forall i \in [0, N_m - 1], \quad (3)$$

where $\mathbb{1}$ is the indicator function that outputs 1 if $(s_i = 1 \wedge s_j = 1)$ and 0 otherwise. This process is integrated into the multi-threaded data preprocessing stage of deep learning frameworks, ensuring it does not affect the training speed.

Progressive Reconstruction	Furthest Sampling	ρ_d	Top-1	FLOPs	Memory	Time
\times	\times	0	81.7	1.00 \times	1.00 \times	1.00 \times
\times	\times	25	81.4 _{-0.3}			
\checkmark	\times	25	81.7	0.85 \times	0.81 \times	0.83 \times
\times	\checkmark	25	81.6			
\checkmark	\checkmark	25	81.7 _{-0.0}			
\times	\times	50	81.1 _{-0.6}			
\checkmark	\times	50	81.6	0.72 \times	0.64 \times	0.75 \times
\times	\checkmark	50	81.4			
\checkmark	\checkmark	50	81.8 _{+0.1}			
\times	\times	65	80.3 _{-1.4}			
\checkmark	\times	65	81.5	0.64 \times	0.55 \times	0.65 \times
\times	\checkmark	65	80.4			
\checkmark	\checkmark	65	81.7 _{-0.0}			

Table 2. Ablation studies on the proposed method. Experiments that mark the furthest sampling as \times use random sampling to throw tokens. All experiments are conducted by pre-training ViT-B/16 [15] on ImageNet-1K [44] for 100 epochs. We count the maximum memory usage and floating-point operations per second (FLOPs) according to a training iteration of a 224×224 image and report the values relative to the baseline method. During pre-training, the progressive reconstruction scheme only increases 7.3×10^{-3} GFLOPs.

In implementation, we use a greedy strategy to find an approximate solution of Eq. (1). Please refer to the supplementary material for more details.

4. Experiments

4.1. Experiment settings

In this work, we apply our proposed method to different frameworks [18, 24, 29, 36, 52, 62] to verify its effectiveness and follow the settings of corresponding official papers. For a fair comparison, we pre-train and fine-tune the models on ImageNet-1K [44] that comprises 1.2 million images and 1,000 categories. Following existing works [24, 64], we mainly use the fully fine-tuning protocol for evaluation. Specifically, we fine-tune ViT-B/16 and ViT-L/16 for 100 and 50 epochs, respectively. Please refer to the supplementary material for more details.

4.2. Experiment results

Tab. 2 examines the effects of the proposed progressive reconstruction scheme and furthest sampling across different throwing ratios ρ_d . For example, the baseline with a token-throwing ratio ρ_d of 50% (*i.e.*, the decoder only operates half of the tokens) significantly reduces the computational costs and accelerates the pre-training but degrades the Top-1 accuracy from 81.7% to 81.1%. In contrast, our proposed method can mitigate this degradation without increasing computational costs, apart from the negligible 7.3×10^{-3} GFLOPs in spatial aggregation. The experiments of different throwing ratios also share a consistent trend, verifying that our method can learn high-quality representations and significantly save costs.

	Architecture	Epochs	ρ_d	Top-1	Flops	Memory
MAE	ViT-B/16	100	0	81.7	1.00 \times	1.00 \times
MAE	ViT-B/16	100	50	81.1	0.72 \times	0.64 \times
+PR-MIM	ViT-B/16	100	50	81.8	0.72 \times	0.64 \times
MAE	ViT-B/16	300	0	82.7	1.00 \times	1.00 \times
MAE	ViT-B/16	300	50	82.3	0.72 \times	0.64 \times
+PR-MIM	ViT-B/16	300	50	82.7	0.72 \times	0.64 \times
MAE	ViT-B/16	800	0	83.3	1.00 \times	1.00 \times
MAE	ViT-B/16	800	50	83.0	0.72 \times	0.64 \times
+PR-MIM	ViT-B/16	800	50	83.3	0.72 \times	0.64 \times
MAE	ViT-L/16	100	0	83.3	1.00 \times	1.00 \times
MAE	ViT-L/16	100	50	82.4	0.87 \times	0.82 \times
+PR-MIM	ViT-L/16	100	50	83.2	0.87 \times	0.82 \times
MAE	ViT-L/16	800	0	85.4	1.00 \times	1.00 \times
+PR-MIM	ViT-L/16	800	50	85.4	0.87 \times	0.82 \times

Table 3. Training schedules and model scaling. PR-MIM means our method.

Training schedules and model scaling. Tab. 3 shows that the proposed method can adapt to longer schedules and larger models. For example, when pre-training ViT-B/16 for 800 epochs, our method achieves performance consistent with the standard MAE, while partial reconstruction reduces the performance by 0.3%. We also observe that larger models are more susceptible to the negative effects of partial reconstruction in Tab. 3 and Tab. 5. When pre-training for 100 epochs, partial reconstruction degrades the performance by 0.6% and 0.9% with ViT-B/16 and ViT-L/16, re-

		Target Epochs	ρ_d	Top-1	FLOPs	Memory
SimMIM [62]		0	81.6	1.00×	1.00×	
SimMIM [62]	RGB	100	30	81.0	0.50×	0.61×
+PR-MIM			30	81.7	0.50×	0.61×
SimMIM [62]	RGB	800	0	83.8	1.00×	1.00×
+PR-MIM			30	83.8	0.50×	0.61×
LocalMIM [52]		0	83.3	1.00×	1.00×	
LocalMIM [52]	HOG	100	65	82.9	0.91×	0.84×
+PR-MIM			65	83.3	0.91×	0.84×
MFF [36]		0	83.6	1.00×	1.00×	
MFF [36]	RGB	800	50	83.3	0.73×	0.64×
+PR-MIM			50	83.8	0.73×	0.64×
TEC [18]		0	84.8	1.00×	1.00×	
TEC [18]	iBOT	300	50	84.5	0.82×	0.81×
+PR-MIM			50	84.7	0.82×	0.81×

Table 4. Compatibility with different methods. Besides MAE [24] in Tab. 2, our method is compatible with different methods.

		Architecture	Epochs	ρ_d	Top-1
GreenMIM [29]				0	83.2
GreenMIM [29]	Swin-B [37]		100	50	82.9
+PR-MIM				50	83.3
GreenMIM [29]				0	83.8
GreenMIM [29]	Swin-L [37]		100	50	83.1
+PR-MIM				50	83.9

Table 5. Compatibility with Swin transformer, where the masking ratio is 0.75.

spectively. But our method mitigates the degradation.

In this work, we mainly focus on the plain vision transformer because it is popular in vision representation learning and needs to save costs more than other architectures due to its high-resolution output. Tab. 5 also shows that our method can apply to other architectures, such as Swin transformer [37]. For instance, partial reconstruction degrades the performance of Swin-B and Swin-L by 0.3% and 0.7% Top-1 accuracy, respectively, and our method can eliminate this. Meanwhile, these results further confirm that larger models may be more susceptible to the negative effects of partial reconstruction.

Generalizing to diverse frameworks. Apart from MAE, the proposed method can be applied to other frameworks, as shown in Tab. 4. We apply our method to MFF [36], GreenMIM [29], TEC [18], and LocalMIM [52] and consistently guarantee the representation quality while reducing the costs. Regarding MFF, our method even improves the Top-1 accuracy by 0.2% when accelerating the training.

SimMIM [62] implements masked image modeling dif-

		Architecture	Epochs	ρ_d	Top-1
MAE			400	40	82.6 [†]
MAE+AMT [38]	ViT-B/16		400	40	82.8
MAE+PR-MIM			400	50	83.0
SimMIM			100	24	81.6
SimMIM+AMT [38]	ViT-B/16		200	24	80.7
SimMIM+PR-MIM			100	30	81.7

Table 6. Comparison with existing partial reconstruction methods. [†] means that the result is borrowed from [38].

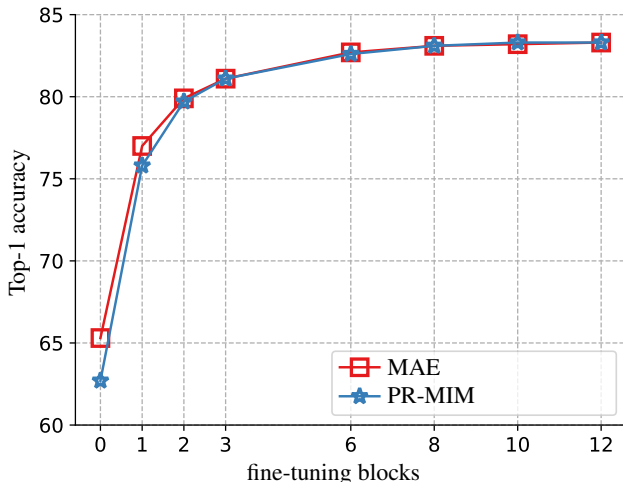


Figure 6. Partial fine-tuning results of ViT-B pre-trained for 800 epochs. Fine-tuning 0 and 12 blocks means the linear probing and fully fine-tuning in Tab. 3, respectively.

ferently from MAE. It accomplishes the representation extraction and token reconstruction in a unified encoder. To apply our method to SimMIM, we throw a subset of masked tokens to reduce the sequence length of the encoder and append the proposed spatial aggregation module after the encoder to reconstruct the thrown tokens. In Tab. 4, we reduce the costs of SimMIM by 50% GFLOPs and 39% memory usage without degrading the performance, demonstrating that our method is orthogonal to different methods.

Comparison with partial reconstruction methods. Tab. 6 compares our method with previous partial reconstruction methods. AMT [38] utilizes attention-driven masking and throwing to mitigate the negative impact of partial reconstruction on performance, but attention maps incur extra computational and storage costs. Moreover, it cannot solve the performance degradation when applying it to SimMIM. Instead, our simple and effective method outperforms AMT using even a higher throwing ratio.

Partial fine-tuning. In this work, we mainly adopt the evaluation protocol of fully fine-tuning models because this protocol is popular in MIM. Experiments show the proposed method can eliminate the performance degradation caused

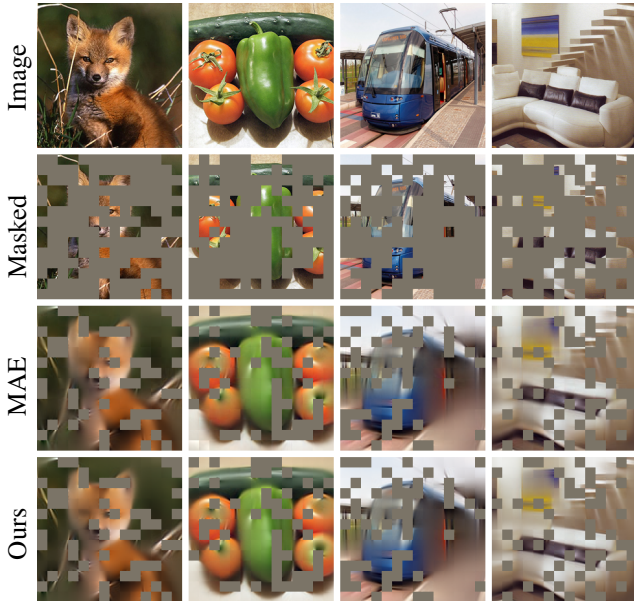


Figure 7. Reconstruction visualization by different methods. The second row shows the unmasked pixels of the original images, and the third row shows the reconstruction results of masked pixels.

	Epochs	ρ_d	IN-C \downarrow	IN-A	IN-R	IN-S
MAE	800	0	51.2	34.6	49.4	35.2
MAE	800	50	51.9	32.9	49.4	36.0
MAE + PR-MIM	800	50	51.4	35.4	49.7	36.4
MFF	800	0	49.0	37.2	51.0	36.8
MFF	800	50	50.5	35.6	51.7	37.6
MFF + PR-MIM	800	50	49.9	37.9	52.1	37.6

Table 7. Robust evaluation. We report Top-1 accuracy apart from IN-C [26], in which we report mean corruption error.

by partial reconstruction when using this protocol. Linear probing is another evaluation protocol. However, pure MIM methods aim at learning powerful nonlinear representations for downstream tasks instead of linearly separable representations. Thus linear probing is inapplicable to evaluate them as analyzed in [24]. Following existing works [24, 64], we also evaluate the models by partial fine-tuning. As shown in Fig. 6, our method does not fully bridge the degradation in linear probing because it does not optimize the linear discriminability of the representations. However, fine-tuning only 2 blocks can eliminate the performance gap. These results, along with the results in Sec. 4.3, show that PR-MIM ensures strong nonlinear representations that are suitable for downstream tasks when accelerating training.

Reconstruction visualization. Fig. 7 shows the reconstruction results when using our method. Compared to standard MAE, we achieve comparable reconstruction quality, showing the effectiveness of the extremely lightweight spatial ag-

	Epochs	ρ_d	iNat ₁₈	iNat ₁₉
MAE	800	0	72.5	78.9
MAE	800	50	71.8	78.2
MAE + PR-MIM	800	50	72.4	79.0
MFF	800	0	73.5	79.8
MFF	800	50	72.5	78.5
MFF + PR-MIM	800	50	73.3	79.8

Table 8. Top-1 accuracy of image classification where iNat₁₈ and iNat₁₉ mean iNaturalist₂₀₁₈ and iNaturalist₂₀₁₉, respectively.

	Epochs	ρ_d	mIoU	mAcc
MAE	800	0	46.8	57.6
MAE	800	50	45.5	56.6
MAE + PR-MIM	800	50	46.9	58.2

Table 9. Semantic segmentation on ADE20K.

gregation module.

4.3. Downstream tasks

We transfer the models pre-trained for 800 epochs on various downstream tasks. The results of baseline MAE are slightly different from those reported in the official papers [24, 34] because the official results use models pre-trained for 1600 epochs. We follow the official implementation to fine-tune models for a fair comparison.

Robustness. In Tab. 7, we evaluate the models, which have been fine-tuned on clean ImageNet-1K, on four corrupted datasets, *i.e.*, ImageNet-A [28], ImageNet-Renditions [27], ImageNet-Sketch [50], and ImageNet-C [26]. Compared to MAE and MFF, partial reconstruction negatively impacts the robustness of ImageNet-A and ImageNet-C. Our method mitigates these robustness issues and even outperforms the MAE and MFF on ImageNet-A. On ImageNet-R and ImageNet-S, partial reconstruction does not degrade the robustness, and our method brings further enhancement.

Transferring on classification. In Tab. 8, we transfer the models to other classification datasets with different domains from ImageNet-1K, including iNaturalist₂₀₁₈ and iNaturalist₂₀₁₉ datasets [49]. Most hyperparameters follow the settings used for ImageNet-1K, except the number of fine-tuning epochs set to 360. Compared to MAE, partial reconstruction degrades the Top-1 accuracy by 0.7% and 0.7% on iNaturalist₂₀₁₈ and iNaturalist₂₀₁₉, respectively. Instead, our method eliminates the degradation and achieves performance comparable to the MAE. There is also a similar trend in comparison with MFF.

Transferring on semantic segmentation. Beyond image-level tasks, we also evaluate the pre-trained models on dense-level tasks like semantic segmentation. We fine-tune the models on ADE20K [68] for 160,000 iterations. Re-

	Epochs	ρ_d	AP ^b	AP ^m
MAE	800	0	51.0	45.2
MAE	800	50	50.2	44.6
MAE + PR-MIM	800	50	50.8	45.2

Table 10. Object detection and instance segmentation segmentation on COCO.

Kernel Size	3×3	5×5	7×7	9×9	11×11
Top-1	81.7	81.7	81.8	81.7	81.6

Table 11. Ablation studies on the kernel sizes in the progressive reconstruction. The ViT-B/16 models are pre-trained on ImageNet-1K for 100 epochs.

garding hyperparameters, we follow the settings in MAE except for the layer-wise learning rate decay, which we set to 0.75 instead of 0.65, as experiments show that a larger layer-wise decay is more suitable for models pre-trained for 800 epochs. For a fair comparison, we also fine-tune the standard MAE with a decay of 0.75 and achieve a mIoU of 46.8%, higher than the 46.1% reported using original settings [36]. However, partial reconstruction degrades the mIoU by 1.3% when throwing 50% of the masked tokens. Our method avoids this issue while keeping the acceleration effect of partial reconstruction.

Transferring on instance segmentation. Following ViT-Det [34], we fine-tune Mask RCNN [22] for 100 epochs with a simple feature pyramid. Meanwhile, we use a batch size of 32 instead of 64 due to the limitation of computational sources, and the learning rate is also reduced by half following the linear scaling rule [20]. As shown in Tab. 10, we report segmentation mask AP^m and bounding box AP^b. Partial reconstruction decreases the AP^b and AP^m by 0.8% and 0.6%, respectively. Instead, our method can mitigate such degradation and achieve performance considerable to the standard MAE. These results on downstream tasks show that our method can maintain the quality of representations in different downstream tasks while significantly reducing pre-training costs.

4.4. Ablation studies

Components. In Tab. 2, we perform ablation studies on the progressive reconstruction scheme and furthest sampling to analyze their impact at different throwing ratios ρ_d . Without them, performance drops as ρ_d increases. Across different throwing ratios, the progressive reconstruction consistently mitigates the performance degradation caused by partial reconstruction, and the furthest sampling also outperforms random sampling. Finally, combining them yields the best results to achieve efficient trade-offs in memory, computation, and performance.

	Top-1	FLOPs
Average pooling	fail	-
Depth-wise convolution	81.8	$7.3 \cdot 10^{-3}G$
Transformer block	81.8	0.65G
ConvNeXt block	81.7	0.41G

Table 12. Different designs of the spatial aggregation module in progressive reconstruction.

Spatial receptive field. Tab. 11 evaluates the impact of different kernel sizes for spatial aggregation within the progressive reconstruction scheme. Results indicate that while kernel sizes 3×3 and 5×5 both yield 81.7% Top-1 accuracy, an increase to 7×7 slightly improves performance to 81.8%. However, further increasing the kernel size to 9×9 and 11×11 does not yield additional gains, with performance slightly decreasing to 81.6%. These results suggest that a moderate local receptive field size, such as 7×7 , is enough for effective reconstruction.

Design of spatial aggregation. We evaluate different designs of spatial aggregation in Tab. 12, including depth-wise convolution, Transformer block, and ConvNeXt block. Among them, the simple depth-wise convolution achieves high accuracy (81.8% Top-1) with minimal cost (only $7.3 \cdot 10^{-3}$ GFLOPs), making it both efficient and effective to reconstruct thrown tokens. Although Transformer and ConvNeXt blocks also yield strong results, they significantly increase FLOPs (0.65G and 0.41G, respectively). Additionally, we try average pooling, a simpler operation, but the model fails to converge due to its inability to model spatial dependencies. Thus, depth-wise convolution is chosen for balancing accuracy and efficiency.

5. Conclusion

In this work, we explore integrating partial reconstruction, a technique that reconstructs only a subset of masked tokens and throws the other ones, into masked image modeling to save pre-training costs without compromising the quality of representations. In response to the issue that partial reconstruction does not utilize each token in pre-training, our proposed progressive reconstruction scheme and furthest sampling effectively reconstruct the tokens thrown by partial reconstruction, ensuring that all tokens are adequately involved in supervision. Importantly, the proposed method increases minimal computational costs and thus preserves the acceleration benefits of partial reconstruction while mitigating the associated performance degradation. Extensive experiments across different downstream tasks demonstrate the effectiveness of our method.

References

- [1] Yuki M. Asano, Christian Rupprecht, and Andrea Vedaldi. Self-labelling via simultaneous clustering and representation learning. In *ICLR*, 2020. 2
- [2] Mahmoud Assran, Quentin Duval, Ishan Misra, Piotr Bojanowski, Pascal Vincent, Michael Rabbat, Yann LeCun, and Nicolas Ballas. Self-supervised learning from images with a joint-embedding predictive architecture. In *CVPR*, 2023. 2
- [3] Hangbo Bao, Li Dong, Songhao Piao, and Furu Wei. BEit: BERT pre-training of image transformers. In *ICLR*, 2022. 2
- [4] Mathilde Caron, Ishan Misra, Julien Mairal, Priya Goyal, Piotr Bojanowski, and Armand Joulin. Unsupervised learning of visual features by contrasting cluster assignments. In *NeurIPS*, 2020. 2
- [5] Mathilde Caron, Hugo Touvron, Ishan Misra, Hervé Jégou, Julien Mairal, Piotr Bojanowski, and Armand Joulin. Emerging properties in self-supervised vision transformers. In *ICCV*, 2021. 2
- [6] Jun Chen, Ming Hu, Boyang Li, and Mohamed Elhoseiny. Efficient self-supervised vision pretraining with local masked reconstruction. *arXiv preprint arXiv:2206.00790*, 2022. 4
- [7] Ting Chen, Simon Kornblith, Mohammad Norouzi, and Geoffrey Hinton. A simple framework for contrastive learning of visual representations. In *ICML*, 2020. 2
- [8] Xinlei Chen and Kaiming He. Exploring simple siamese representation learning. In *CVPR*, 2021. 2
- [9] Xiaokang Chen, Mingyu Ding, Xiaodi Wang, Ying Xin, Shentong Mo, Yunhao Wang, Shumin Han, Ping Luo, Gang Zeng, and Jingdong Wang. Context autoencoder for self-supervised representation learning. *IJCV*, 132(1):208–223, 2024. 2
- [10] N. Dalal and B. Triggs. Histograms of oriented gradients for human detection. In *CVPR*, 2005. 2
- [11] Jacob Devlin, Ming-Wei Chang, Kenton Lee, and Kristina Toutanova. Bert: Pre-training of deep bidirectional transformers for language understanding. In *NAACL-HLT*, 2019. 2
- [12] Carl Doersch, Abhinav Gupta, and Alexei A. Efros. Unsupervised visual representation learning by context prediction. In *ICCV*, 2015. 2
- [13] Xiaoyi Dong, Jianmin Bao, Ting Zhang, Dongdong Chen, Weiming Zhang, Lu Yuan, Dong Chen, Fang Wen, and Nenghai Yu. Bootstrapped masked autoencoders for vision bert pretraining. In *ECCV*, 2022. 2
- [14] Xiaoyi Dong, Jianmin Bao, Ting Zhang, Dongdong Chen, Weiming Zhang, Lu Yuan, Dong Chen, Fang Wen, Nenghai Yu, and Baining Guo. Peco: Perceptual codebook for bert pre-training of vision transformers. In *AAAI*, 2023. 2
- [15] Alexey Dosovitskiy, Lucas Beyer, Alexander Kolesnikov, Dirk Weissenborn, Xiaohua Zhai, Thomas Unterthiner, Mostafa Dehghani, Matthias Minderer, Georg Heigold, Sylvain Gelly, Jakob Uszkoreit, and Neil Houlsby. An image is worth 16x16 words: Transformers for image recognition at scale. In *ICLR*, 2021. 2, 5
- [16] Debidatta Dwivedi, Yusuf Aytar, Jonathan Tompson, Pierre Sermanet, and Andrew Zisserman. With a little help from my friends: Nearest-neighbor contrastive learning of visual representations. In *ICCV*, 2021. 2
- [17] Aleksandr Ermolov, Aliaksandr Siarohin, Enver Sangineto, and Nicu Sebe. Whitening for self-supervised representation learning. In *ICML*, 2021. 2
- [18] Shanghua Gao, Pan Zhou, Ming-Ming Cheng, and Shuicheng Yan. Towards sustainable self-supervised learning. *arXiv preprint arXiv:2210.11016*, 2022. 2, 5, 6
- [19] Spyros Gidaris, Praveer Singh, and Nikos Komodakis. Unsupervised representation learning by predicting image rotations. In *ICLR*, 2018. 2
- [20] Priya Goyal, Piotr Dollár, Ross Girshick, Pieter Noordhuis, Lukasz Wesolowski, Aapo Kyrola, Andrew Tulloch, Yangqing Jia, and Kaiming He. Accurate, large minibatch sgd: Training imagenet in 1 hour. *arXiv preprint arXiv:1706.02677*, 2018. 8
- [21] Jean-Bastien Grill, Florian Strub, Florent Altché, Corentin Tallec, Pierre H. Richemond, Elena Buchatskaya, Carl Doersch, Bernardo Ávila Pires, Zhaohan Guo, Mohammad Gheshlaghi Azar, Bilal Piot, Koray Kavukcuoglu, Rémi Munos, and Michal Valko. Bootstrap your own latent - a new approach to self-supervised learning. In *NeurIPS*, 2020. 2
- [22] Kaiming He, Georgia Gkioxari, Piotr Dollar, and Ross Girshick. Mask r-cnn. In *ICCV*, 2017. 8
- [23] Kaiming He, Haoqi Fan, Yuxin Wu, Saining Xie, and Ross Girshick. Momentum contrast for unsupervised visual representation learning. In *CVPR*, 2020. 2
- [24] Kaiming He, Xinlei Chen, Saining Xie, Yanghao Li, Piotr Dollár, and Ross Girshick. Masked autoencoders are scalable vision learners. In *CVPR*, 2022. 1, 2, 3, 5, 6, 7
- [25] Olivier J. Hénaff, Skanda Koppula, Jean-Baptiste Alayrac, Aaron van den Oord, Oriol Vinyals, and João Carreira. Efficient visual pretraining with contrastive detection. In *ICCV*, 2021. 2
- [26] Dan Hendrycks and Thomas Dietterich. Benchmarking neural network robustness to common corruptions and perturbations. *ICLR*, 2019. 7
- [27] Dan Hendrycks, Steven Basart, Norman Mu, Saurav Kadavath, Frank Wang, Evan Dorundo, Rahul Desai, Tyler Zhu, Samyak Parajuli, Mike Guo, Dawn Song, Jacob Steinhardt, and Justin Gilmer. The many faces of robustness: A critical analysis of out-of-distribution generalization. In *ICCV*, 2021. 7
- [28] Dan Hendrycks, Kevin Zhao, Steven Basart, Jacob Steinhardt, and Dawn Song. Natural adversarial examples. In *CVPR*, 2021. 7
- [29] Lang Huang, Shan You, Mingkai Zheng, Fei Wang, Chen Qian, and Toshihiko Yamasaki. Green hierarchical vision transformer for masked image modeling. In *NeurIPS*, 2022. 2, 5, 6
- [30] Zhicheng Huang, Xiaojie Jin, Chengze Lu, Qibin Hou, Ming-Ming Cheng, Dongmei Fu, Xiaohui Shen, and Jiashi Feng. Contrastive masked autoencoders are stronger vision learners. *IEEE TPAMI*, 46(4):2506–2517, 2024. 2
- [31] Soroush Abbasi Koohpayegani, Ajinkya Tejankar, and Hamed Pirsiavash. Mean shift for self-supervised learning. In *ICCV*, 2021. 2

- [32] Gustav Larsson, Michael Maire, and Gregory Shakhnarovich. Colorization as a proxy task for visual understanding. In *CVPR*, 2017. 2
- [33] Gang Li, Heliang Zheng, Daqing Liu, Chaoyue Wang, Bing Su, and Changwen Zheng. Semmae: Semantic-guided masking for learning masked autoencoders. In *NeurIPS*, 2022. 2
- [34] Yanghao Li, Hanzi Mao, Ross Girshick, and Kaiming He. Exploring plain vision transformer backbones for object detection. In *ECCV*, 2022. 7, 8
- [35] Zhong-Yu Li, Shanghua Gao, and Ming-Ming Cheng. Sere: Exploring feature self-relation for self-supervised transformer. *IEEE TPAMI*, 45(12):15619–15631, 2023. 2
- [36] Yuan Liu, Songyang Zhang, Jiacheng Chen, Zhaohui Yu, Kai Chen, and Dahua Lin. Improving pixel-based mim by reducing wasted modeling capability. In *ICCV*, 2023. 2, 5, 6, 8
- [37] Ze Liu, Yutong Lin, Yue Cao, Han Hu, Yixuan Wei, Zheng Zhang, Stephen Lin, and Baining Guo. Swin transformer: Hierarchical vision transformer using shifted windows. *ICCV*, 2021. 6
- [38] Zhengqi Liu, Jie Gui, and Hao Luo. Good helper is around you: attention-driven masked image modeling. In *AAAI*, 2023. 1, 3, 6
- [39] Jiawei Mao, Shujian Guo, Yuanqi Chang, Xuesong Yin, and Binling Nie. Medical supervised masked autoencoders: Crafting a better masking strategy and efficient fine-tuning schedule for medical image classification. *arXiv preprint arXiv:2305.05871*, 2023. 1, 3
- [40] Mehdi Noroozi and Paolo Favaro. Unsupervised learning of visual representations by solving jigsaw puzzles. In *ECCV*, 2016. 2
- [41] Mehdi Noroozi, Hamed Pirsiavash, and Paolo Favaro. Representation learning by learning to count. In *ICCV*, 2017. 2
- [42] Deepak Pathak, Philipp Krahenbuhl, Jeff Donahue, Trevor Darrell, and Alexei A. Efros. Context encoders: Feature learning by inpainting. In *CVPR*, 2016. 2
- [43] Byungseok Roh, Wuhyun Shin, Ildoo Kim, and Sungwoong Kim. Spatilly consistent representation learning. In *CVPR*, 2021. 2
- [44] Olga Russakovsky, Jia Deng, Hao Su, Jonathan Krause, Sanjeev Satheesh, Sean Ma, Zhiheng Huang, Andrej Karpathy, Aditya Khosla, Michael Bernstein, et al. Imagenet large scale visual recognition challenge. *IJCV*, 115(3):211–252, 2015. 5
- [45] Chenxin Tao, Xizhou Zhu, Weijie Su, Gao Huang, Bin Li, Jie Zhou, Yu Qiao, Xiaogang Wang, and Jifeng Dai. Siamese image modeling for self-supervised vision representation learning. In *CVPR*, 2023. 2
- [46] Keyu Tian, Yi Jiang, Qishuai Diao, Chen Lin, Liwei Wang, and Zehuan Yuan. Designing bert for convolutional networks: Sparse and hierarchical masked modeling. In *ICLR*, 2023. 2
- [47] Yuandong Tian, Xinlei Chen, and Surya Ganguli. Understanding self-supervised learning dynamics without contrastive pairs. In *ICML*, 2020. 2
- [48] Yunjie Tian, Lingxi Xie, Zhaozhi Wang, Longhui Wei, Xiaopeng Zhang, Jianbin Jiao, Yaowei Wang, Qi Tian, and Qixiang Ye. Integrally pre-trained transformer pyramid networks. In *CVPR*, 2023. 2
- [49] Grant Van Horn, Oisín Mac Aodha, Yang Song, Yin Cui, Chen Sun, Alex Shepard, Hartwig Adam, Pietro Perona, and Serge Belongie. The inaturalist species classification and detection dataset. In *CVPR*, 2018. 7
- [50] Haohan Wang, Songwei Ge, Zachary Lipton, and Eric P Xing. Learning robust global representations by penalizing local predictive power. In *NeurIPS*, 2019. 7
- [51] Haochen Wang, Kaiyou Song, Junsong Fan, Yuxi Wang, Jin Xie, and Zhaoxiang Zhang. Hard patches mining for masked image modeling. In *CVPR*, 2023. 2
- [52] Haoqing Wang, Yehui Tang, Yunhe Wang, Jianyuan Guo, Zhi-Hong Deng, and Kai Han. Masked image modeling with local multi-scale reconstruction. In *CVPR*, 2023. 2, 5, 6
- [53] Limin Wang, Bingkun Huang, Zhiyu Zhao, Zhan Tong, Yinan He, Yi Wang, Yali Wang, and Yu Qiao. Videomae v2: Scaling video masked autoencoders with dual masking. In *CVPR*, 2023. 1, 3
- [54] Wenhui Wang, Hangbo Bao, Li Dong, Johan Bjorck, Zhiliang Peng, Qiang Liu, Kriti Aggarwal, Owais Khan Mohammed, Saksham Singhal, Subhojit Som, and Furu Wei. Image as a foreign language: BEiT pretraining for vision and vision-language tasks. In *CVPR*, 2023. 2
- [55] Xinlong Wang, Rufeng Zhang, Chunhua Shen, Tao Kong, and Lei Li. Dense contrastive learning for self-supervised visual pre-training. In *CVPR*, 2021. 2
- [56] Chen Wei, Haoqi Fan, Saining Xie, Chao-Yuan Wu, Alan Yuille, and Christoph Feichtenhofer. Masked feature prediction for self-supervised visual pre-training. In *CVPR*, 2022. 2
- [57] Longhui Wei, Lingxi Xie, Wengang Zhou, Houqiang Li, and Qi Tian. Mvp: Multimodality-guided visual pre-training. In *ECCV*, 2022. 2
- [58] Sanghyun Woo, Shoubhik Debnath, Ronghang Hu, Xinlei Chen, Zhuang Liu, In So Kweon, and Saining Xie. Convnext v2: Co-designing and scaling convnets with masked autoencoders. In *CVPR*, 2023. 2
- [59] Zhirong Wu, Yuanjun Xiong, Stella X. Yu, and Dahua Lin. Unsupervised feature learning via non-parametric instance discrimination. In *CVPR*, 2018. 2
- [60] Jiahao Xie, Wei Li, Xiaohang Zhan, Ziwei Liu, Yew Soon Ong, and Chen Change Loy. Masked frequency modeling for self-supervised visual pre-training. In *ICLR*, 2023. 2
- [61] Zhenda Xie, Yutong Lin, Zheng Zhang, Yue Cao, Stephen Lin, and Han Hu. Propagate yourself: Exploring pixel-level consistency for unsupervised visual representation learning. In *CVPR*, 2021. 2
- [62] Zhenda Xie, Zheng Zhang, Yue Cao, Yutong Lin, Jianmin Bao, Zhuliang Yao, Qi Dai, and Han Hu. Simmim: A simple framework for masked image modeling. In *CVPR*, 2022. 1, 2, 5, 6
- [63] Chun-Hsiao Yeh, Cheng-Yao Hong, Yen-Chi Hsu, Tyng-Luh Liu, Yubei Chen, and Yann LeCun. Decoupled contrastive learning. In *ECCV*, 2022. 2
- [64] Kun Yi, Yixiao Ge, Xiaotong Li, Shusheng Yang, Dian Li, Jianping Wu, Ying Shan, and Xiaohu Qie. Masked image modeling with denoising contrast. *ICLR*, 2023. 2, 5, 7

- [65] Jure Zbontar, Li Jing, Ishan Misra, Yann LeCun, and Stéphane Deny. Barlow twins: Self-supervised learning via redundancy reduction. In *PMLR*, 2021. [2](#)
- [66] Richard Zhang, Phillip Isola, and Alexei A Efros. Colorful image colorization. In *ECCV*, 2016. [2](#)
- [67] Yucheng Zhao, Guangting Wang, Chong Luo, Wenjun Zeng, and Zheng-Jun Zha. Self-supervised visual representations learning by contrastive mask prediction. In *ICCV*, 2021. [2](#)
- [68] Bolei Zhou, Hang Zhao, Xavier Puig, Sanja Fidler, Adela Barriuso, and Antonio Torralba. Scene parsing through ade20k dataset. In *CVPR*, 2017. [7](#)
- [69] Jinghao Zhou, Chen Wei, Huiyu Wang, Wei Shen, Cihang Xie, Alan Yuille, and Tao Kong. ibot: Image bert pre-training with online tokenizer. In *ICLR*, 2022. [2](#)
- [70] Pan Zhou, Yichen Zhou, Chenyang Si, Weihao Yu, Teck Khim Ng, and Shuicheng Yan. Mugs: A multi-granular self-supervised learning framework. In *arXiv preprint arXiv:2203.14415*, 2022. [2](#)

PR-MIM: Delving Deeper into Partial Reconstruction in Masked Image Modeling

Supplementary Material

Algorithm 1: Furthest sampling

```
Data:  $\mathbf{D} \in \mathbb{R}^{N_m \times N_m}$ ,  $N_m$ , and  $N_t$   
Result:  $s \in \mathbb{R}^{N_m}$   
 $s \leftarrow \{0\}_{N_m}$ ; /* Initialization */  
 $tokens \leftarrow \text{empty\_set}()$   
  
 $i \leftarrow \text{randoint}(0, N_m - 1)$ ; /* Choose the  
first retained token */  
 $s_i \leftarrow 1$ ;  
 $tokens.append(i)$   
  
for  $k \leftarrow 1$  to  $N_m - N_t - 1$  do  
     $\hat{\mathbf{D}} \leftarrow \mathbf{D}_{[:,tokens]} \in \mathbb{R}^{N_m \times k}$ ; /* Columns  
    corresponding to retained  
    tokens */  
  
     $i \leftarrow \arg \max_i \left\{ \min(\hat{\mathbf{D}}, \text{axis} = 1) \right\}$ ; /* The  
    i-th token is retained */  
  
     $s_i \leftarrow 1$ ;  
     $tokens.append(i)$   
end
```

6. Implementation of furthest sampling

Given N_m masked tokens, the furthest sampling throws N_t tokens and retains $N_m - N_t$ tokens. In implementation, we use a greedy strategy to find the approximate solution of Eq. (1) of the manuscript, as shown in Alg. 1. After the first retained token is chosen by random sampling, this process iteratively retains a new token that is furthest from the already retained tokens, ensuring a dispersed selection of retained tokens.

7. Implementation details

Tab. 13 and Tab. 14 summarize the hyperparameters used for pre-training and fine-tuning, respectively. These hyperparameters are used for MAE-based experiments, and the other experiments follow the official settings of the corresponding papers. For fine-tuning, the learning rate and layer-wise learning-rate decay rate are slightly different from the official paper of MAE and are adjusted to be consistent with the official codes. This is because the official codes of MAE use normalized pixels as the reconstruction targets, but the official paper uses raw pixels as the default

Table 13. Pre-training details.

item	value
optimizer	AdamW ($\beta_1 = 0.9$ and $\beta_2 = 0.95$)
base learning rate	1.5e-4
learning rate	2.4e-3
weight decay	0.05
batch size	4096
warmup epochs	40
epochs	100/300/800
mask ratio	0.75
norm pixel loss	True
learning rate schedule	cosine decay

Table 14. Fine-tuning details.

item	value
optimizer	AdamW ($\beta_1 = 0.9$ and $\beta_2 = 0.999$)
base learning rate	5e-4(B),1e-3(L)
learning rate	2e-3(B),4e-3(L)
weight decay	0.05
batch size	1024
warmup epochs	5
epochs	100 (B),50 (L)
layer-wise lr decay	0.65(B),0.75(L)
drop-path rate	0.1 (B),0.2(L)
data augmentation	RandAug (9, 0.5)
reprob	0.25
mixup	0.8
cutmix	1.0
label smoothing	0.1
learning rate schedule	cosine decay

setting. Using normalized pixels achieves a better performance, thus we follow the settings of official codes.